

# Fractal Characteristics of Free Surface Profiles of Metal Sheets under Equi-Biaxial Tension\*

Yasushi KUROSAKI\*\*, Masahito MATSUI\*\*,  
Tomoyuki TAKAYAMA\*\*\* and Akira NAKANISHI\*\*\*\*

Free surface profiles of aluminum sheets under equi-biaxial tension are examined by employing three kinds of fractal analyses, i.e., the zeroset, power spectrum and box-counting methods. With an increase in plastic strain, long-wavelength components of the surface profiles become dominant, and their fractal structure tends to become constant beyond a certain strain. It is found that both surface roughness and fractal dimensions depend on the equivalent strain, independent of the stress ratio. A method for simulating the surface roughening behavior is presented by utilizing the power spectrum method.

**Key Words:** Plastic Forming, Surface Roughness, Press Working, Fractal, Self-Affinity, Sheet Metal, Free Surface, Equi-Biaxial Tension

## 1. Introduction

In sheet metal forming, the phenomenon of surface roughening due to plastic deformation is closely related to various surface problems, i.e., forming limit (necking caused by surface imperfection), coating feasibility, surface quality of products, galling and other friction characteristics. Thus, many studies on this phenomenon have been carried out, employing surface roughness as a characteristic measure and examining its relationship with plastic strain<sup>(1)~(3)</sup>. However, the detailed geometry of a new surface formed by plastic deformation has not been investigated; thus, its actual state remains unclear. One of the reasons for this is that surface profiles involve various classes of randomness and are difficult to characterize quantitatively. In our previous research<sup>(4)</sup> we established a fractal concept, and presented three analyti-

cal methods, thereby clarifying fractal characteristics on free surface profiles of aluminum sheets under uniaxial tension.

In the present study, using a similar approach to that used in the aforementioned research, fractals are shown on free surface profiles of aluminum sheets under equi-biaxial tension, and their dependence on the tensile method (stress ratio) and strain is examined. A method for simulating the variation of surface roughening with strain is also presented.

## 2. Determination of Fractal Dimensions

A fractal property is usually characterized by the fractal dimensions. In general, fractal dimensions of solid surfaces are regarded as a means of expressing an apparent complexity (randomness) in their geometries or of estimating their area. Although various methods for determining fractal dimensions had been attempted in past investigations, no general methods have been established, and theoretical relations among obtained dimensions remain to be solved. Accordingly, fractal dimensions are determined tentatively in the present study, based on three kinds of analyses presented in the previous investigation<sup>(4)</sup>. Here, it should be noted that in general, solid surfaces are not self-similar, but self-affine. Nonuniform scaling, where shapes are invariant under

\* Received 4th March, 1998. Japanese original: Trans. Jpn. Soc. Mech. Eng., Vol. 63, No. 613, C(1997), p. 3265-3271 (Received 13th November, 1996)

\*\* Faculty of Engineering, Mie University, 1515 Kamihama-cho, Tsu, Mie 514-8507, Japan

\*\*\* Graduate School of Engineering, Mie University, 1515 Kamihama-cho, Tsu, Mie 514-8507, Japan

\*\*\*\* Shinko Denki Co., Ltd., Ise Factory, 100 Takegahana-cho, Ise, Mie 516-8550, Japan

transformations that scale different coordinates by different amounts, is known as self-affinity. While the zerset and power spectrum methods to be mentioned in the following are regarded as applicable to self-affine surfaces, the box-counting method, which has been employed in conventional applications, is based on a self-similarity assumption and is inadequate for use with solid surfaces<sup>(5)</sup>. However, this method is still convenient for estimating relative complexity of surfaces and is therefore also used here.

### 2.1 Zerset method

Intersections of surface irregularities and the basal plane, referred to as zerset elements here, are generated and their shapes are directly observed, as shown in Fig. 1. Even if surfaces are self-affine, if they are isotropic in-plane, the resultant zerset elements become self-similar and reduce their fractal dimensions by one<sup>(6)</sup>. When the area and the peripheral length of each zerset element are denoted by  $A_z$  and  $L_z$ , respectively, and  $L_z$  has the dimension  $D_z$ , the following is obtained from the measure-dimension relation<sup>(7)</sup>.

$$A_z^{1/2} \propto L_z^{1/D_z} \quad (1)$$

When the relation between  $L_z$  and  $A_z$  is measured experimentally, the zerset dimension  $D_z$  can be determined as  $D_z = 2/\alpha_z$  from the slope of the  $\log(L_z)$  vs.  $\log(A_z)$  plot, denoted by  $\alpha_z$ .

### 2.2 Power spectrum method

The power spectra  $S_P$  and the wavelengths  $\lambda$  are obtained by applying FFT analysis to the surface profile curves, and the relation  $S_P \propto \lambda^{-\beta}$  is assumed. The power spectrum dimension  $D_{PS}$  can be determined from the slope of the  $\log(S_P)$  vs.  $\log(\lambda)$  plot, denoted by  $\beta$ , as follows<sup>(8)</sup>:

$$\left. \begin{aligned} D_{PS} &= 2, & 0 \leq \beta < 1 \\ D_{PS} &= E + (3 - \beta)/2, & 1 \leq \beta \leq 3 \\ D_{PS} &= 1, & 3 < \beta \end{aligned} \right\} \quad (2)$$

where  $E$  is the Euclidean dimension, and  $E=1$  in this study.

### 2.3 Box-counting method

The surface profile curves are closely covered with boxes of specified shapes and sizes<sup>(9)</sup>. While the shapes of boxes are similar, their sizes are varied (52 kinds of boxes were used in this study). The following relation is assumed between the covered box number  $N$  and its side length  $r$ .

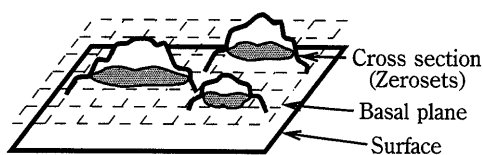


Fig. 1 Schematic explanation of zerset method

$$N \propto r^{-D_B} \quad (3)$$

The box dimension  $D_B$  can be determined as  $D_B = -\alpha_B$  from the slope of the  $\log(N)$  vs.  $\log(r)$  plot, denoted by  $\alpha_B$ . Since the  $D_B$  value depends on the box shape, two shapes, square and rectangular, were employed; their width vs. height ratios were selected as 1 : 1 and 1 : 2.36 on the graphic plane, respectively.

## 3. Experimental Procedure

### 3.1 Material and equi-biaxial tension test

The tested materials were commercially pure aluminum sheets (A 1100-O, 0.8 mm thick, crystal grain size  $17 \mu\text{m}$ ). Their uniaxial properties are shown in Table 1. The initial surface roughnesses of the sheets (maximum height roughness  $R_y$ ) were  $0.53 \mu\text{m}$  and  $2.13 \mu\text{m}$  in the directions parallel and perpendicular to the rolling direction, respectively. The outline of the equi-biaxial tension test is illustrated in Fig. 2. While circular plates 100 mm in diameter were machined from the original aluminum sheets, circular driving plates of the same size were made of killed steel sheets (0.8 mm thick) and in each of these sheets a 10-mm-diameter hole was bored at the center. After the driving plate was put on the aluminum plate (specimen), both were stretch-formed with a flat-headed punch 36 mm in diameter and 4 mm in profile radius. The interface between the punch and the driving plate was lubricated with graphite grease. The stretch-forming test was carried out by means of the sheet metal forming machine under 0.2 mm/s punch speed. These conditions were found to be

Table 1 Uniaxial properties of A 1100

Direction	Tensile strength MPa	N-value*	F-value* MPa	r-value	Total elongation %
0°	103	0.27	193	0.66	27.1
45°	95	0.27	176	1.18	32.8
90°	99	0.28	187	0.66	33.1
Mean	99	0.27	185	0.92	31.5

$$* : \sigma = F \varepsilon^N$$

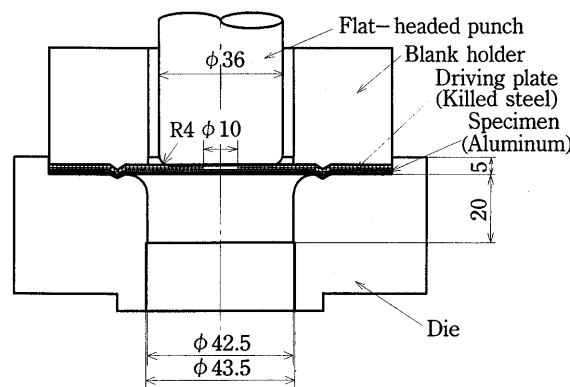


Fig. 2 Equi-biaxial tension test

sufficient for deforming the flat head region of specimens until the initiation of localized necking.

### 3.2 Generation and measurement of zerset elements

In order to estimate the zerset dimension  $D_z$ , small square pieces of 12 mm side length were cut out from the flat head region of specimens, and their lower free surfaces (see Fig. 2) were lapped on a precision lapping plate ( $0.04 \mu\text{m } R_y$ ) with fine diamond powder ( $0.125 \mu\text{m}$  nominal grain size); thus, the zerset elements were generated. Extreme care was taken not to cut the valley walls of surface irregularities during lapping. The zerset elements were observed at the central region of the test pieces within a circle of 10 mm diameter through an optical microscope and a CCD camera. After signals of the magnified images were transferred to an image processor and processed into binary images, the area  $A_z$  and the peripheral length  $L_z$  of each zerset element were measured. One picture involved  $512 \times 512$  pixels, and each pixel was calibrated as  $2.33 \times 2.33 \mu\text{m}^2$ .

### 3.3 Measurement of surface profile curves

In order to estimate the dimensions  $D_{FS}$  and  $D_B$ , surface profile data were obtained under the no cutoff condition by means of a stylus profilometer (Talysurf 10), and their signals were digitized and transferred to a computer. The stylus end surface was flat and square ( $2.5 \times 2.5 \mu\text{m}^2$ ). The resolution of this measuring apparatus was estimated under the nominal magnifications of  $\times 1000$  and  $\times 20$  as  $0.0174 \mu\text{m}$  and  $2.054 \mu\text{m}$  in the vertical and traverse directions, respectively. Measurement of the profile curves was carried out three times for each of the two directions, parallel and perpendicular to the rolling direction, on the lower free surface of the specimen shown in Fig. 2. These respective directions will be denoted by  $0^\circ$  and  $90^\circ$  hereafter.

## 4. Results and Discussion

### 4.1 Surface roughening behavior

Surface curves recorded in the  $90^\circ$  direction are exemplified in Fig. 3. In the present experiment, when the equivalent strain  $\epsilon_{eq}$  exceeded 0.71, a trough with a width near the sheet thickness appeared on the specimen surface, parallel to the  $0^\circ$  direction. Accordingly, this value was regarded as the critical strain of necking initiation. From Hill's anisotropic theory, the equivalent strain  $\epsilon_{eq}$  in equi-biaxial tension is expressed as  $\epsilon_{eq} = \sqrt{(1+r)/2} |\epsilon_t|$ , where  $r$  is the anisotropic parameter called an  $r$ -value, and  $\epsilon_t$  is the thickness strain. Referring to Table 1 and using the in-plane mean  $r$ -value of 0.92, the relation  $\epsilon_{eq} = 0.97 |\epsilon_t|$  is obtained; thus, the difference between  $\epsilon_{eq}$  and  $|\epsilon_t|$  is small. Furthermore, it was pointed out that Hill's

anisotropic theory is inadequate for aluminum sheets<sup>(10)</sup>. For these reasons, the equivalent strain was estimated by  $\epsilon_{eq} = |\epsilon_t|$ , assuming an isotropic material.

Variations of surface roughness (maximum height  $R_y$ ) with tensile strains  $\epsilon_u$  (uniaxial) and  $\epsilon_b (= |\epsilon_t|/2$ , equi-biaxial) are shown in Fig. 4(a), where  $R_y$  values in uniaxial tension were measured for the specimens elongated in the  $0^\circ$  direction. It is seen from Fig. 4(a) that within a certain strain level the  $R_y$  value increases linearly with increasing strains under the respective tensile methods (stress ratios). However, the construction of  $R_y$  vs.  $\epsilon_{eq}$  plots gives a single relation including two tensile methods, except for the steep increase in  $R_y$  due to the occurrence of necking, as shown in Fig. 4(b). Such a result that the dependence of  $R_y$  on the strain can be expressed as a

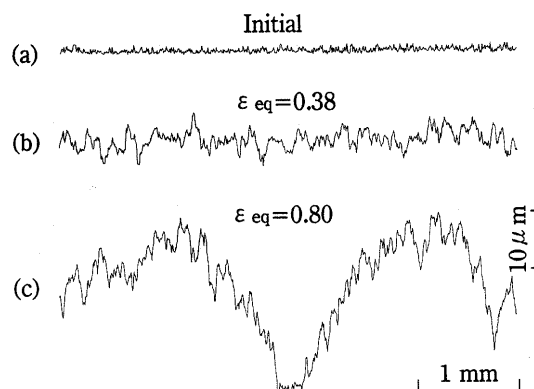
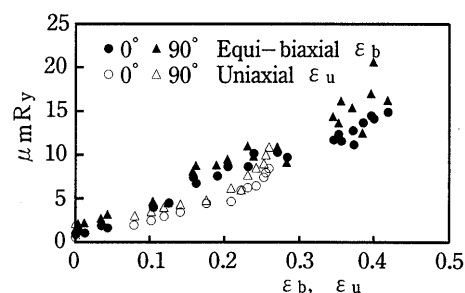
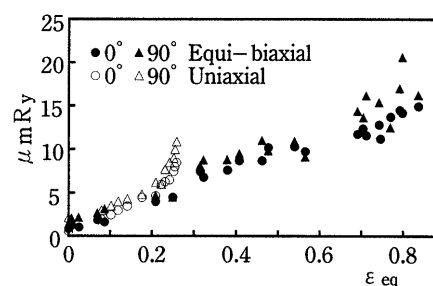


Fig. 3 Examples of recorded surface profiles ( $90^\circ$  direction)



(a)  $R_y$  vs.  $\epsilon_b$  and  $\epsilon_u$



(b)  $R_y$  vs.  $\epsilon_{eq}$

Fig. 4 Relationship between surface roughness  $R_y$  and various strains

unified relation irrespective of the stress ratio by employing  $\epsilon_{eq}$  was reported previously by Yamaguchi et al<sup>(2)</sup>.

**4.2 Zerose dimension**

Images of the zerose elements obtained in the equi-biaxial tension test are exemplified in Fig. 5, where the white parts correspond to the zerose elements. The relative cutting height denoted by  $\delta$  is defined as  $\delta = (R_{y0} - R_{yc}) / R_{y0} \times 100 (\%)$ , where  $R_{y0}$  and  $R_{yc}$  are the surface roughness before and after cutting, respectively. An example of the log-log plots of the peripheral lengths  $L_z$  vs. areas  $A_z$  measured for the zerose elements is shown in Fig. 6, where a linear relation is observed, indicating that the zerose elements follow a fractal geometry. In this study, considering pixel resolution, the zerose dimension  $D_z$

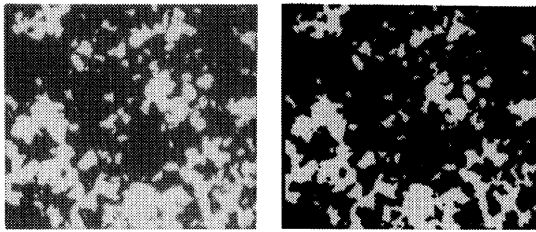


Fig. 5 Example of image of zerose plane ( $\epsilon_{eq} = 0.44$ ,  $\delta = 36.8\%$ )

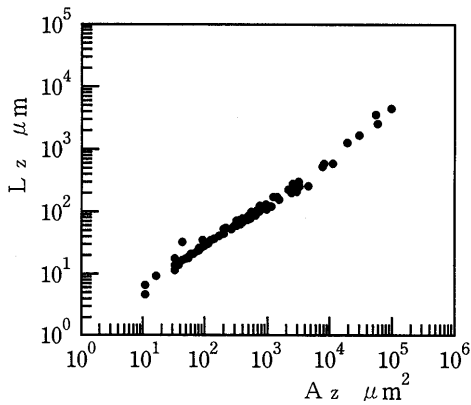


Fig. 6 Relationship between peripheral length  $L_z$  and area  $A_z$  of zerose elements ( $\epsilon_{eq} = 0.44$ ,  $\delta = 36.8\%$ )

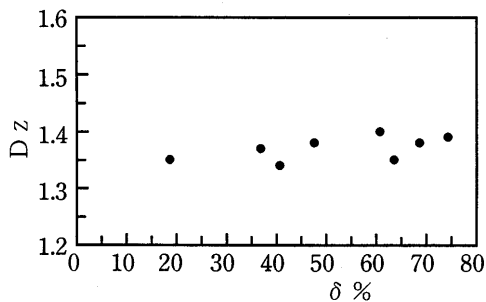


Fig. 7 Relationship between  $D_z$  and relative cutting height  $\delta$  ( $\epsilon_{eq} = 0.44$ )

was determined in the range  $A_z \geq 20 \mu\text{m}^2$ . The relation between  $D_z$  and  $\delta$  is shown in Fig. 7, indicating that  $D_z$  is nearly constant and independent of  $\delta$ ; thus, each asperity of the surface has a uniform fractal structure. Mean values of  $D_z$  for 6 - 8 kinds of  $\delta$  are denoted by  $\bar{D}_z$ , and their relation with equivalent strain  $\epsilon_{eq}$  is shown in Fig. 8.  $\bar{D}_z$  decreases with increasing  $\epsilon_{eq}$  and attains a nearly constant value of 1.35 beyond  $\epsilon_{eq} \approx 0.1$ .  $\bar{D}_z$  values in the case of uniaxial tension are added to Fig. 8, and it is noted that  $\bar{D}_z$  can be plotted on a certain unique curve throughout the uniaxial and equi-biaxial tensions by using  $\epsilon_{eq}$ . A similar result has been obtained with regard to  $R_y$ , as seen in the previous section.

**4.3 Power spectrum dimension**

Log-log plots of the power spectra  $S_P$  and wavelengths  $\lambda$  are exemplified in Fig. 9, where  $S_P$  values are expressed by the measured spectra divided by the measurement time (53.2 s). A linear relation which shows an inflection at  $\lambda \approx 100 \mu\text{m}$  is observed; thus,  $S_P$  follows a multifractal property. Similar phenomena to this were always seen irrespective of the measurement direction of surface profile curves and the strains. The transitional wavelength at the inflection point was found to be nearly constant ( $\lambda \approx 100 \mu\text{m}$ ), but the reason for this is unclear at present. In the range of  $\lambda$  longer than  $100 \mu\text{m}$ , denoted by the region

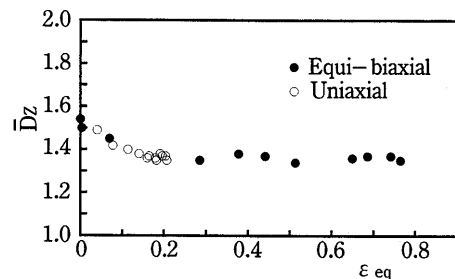


Fig. 8 Relationship between  $\bar{D}_z$  and equivalent strain  $\epsilon_{eq}$

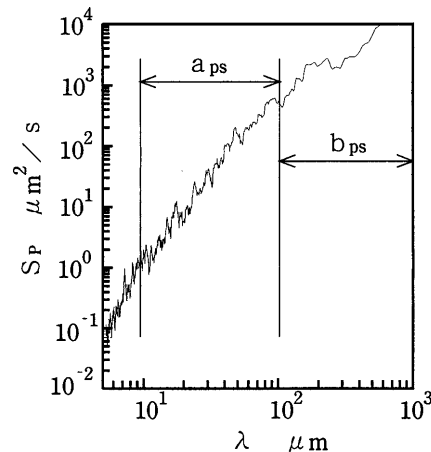


Fig. 9 Relationship between power spectrum  $S_P$  and wavelength  $\lambda$  ( $90^\circ$ ,  $\epsilon_{eq} = 0.57$ )

$b_{PS}$  in Fig. 9,  $\beta \leq 1$  ( $D_{PS}=2$ ) was always found, indicating that a variation in  $\beta$  has no effect on  $D_{PS}$ . A limit of the shorter wavelength was specified as  $10 \mu\text{m}$ , taking into account an error due to the geometry of the stylus profilometer. Finally, the power spectrum dimension  $D_{PS}$  was estimated for  $\lambda$  ranging from  $10 \mu\text{m}$  to  $100 \mu\text{m}$ .

The relation between  $D_{PS}$  and  $\epsilon_{eq}$  is shown in Fig. 10.  $D_{PS}$  decreases with increasing  $\epsilon_{eq}$ , and attains a nearly constant value of 1.1 beyond  $\epsilon_{eq}=0.1$  in the  $0^\circ$  direction or beyond  $\epsilon_{eq}=0.3$  in the  $90^\circ$  direction. With an increase in  $\epsilon_{eq}$ , the difference between  $D_{PS}$  values in the two directions decreases, suggesting that the fractal of surface profiles tends to be in-plane isotropic.

**4.4 Box dimension**

Log-log plots of the covered box number  $N$  and the box width  $r$ , obtained from the surface profile curves, are shown in Fig. 11, where a linear relation showing an inflection at the I.P. point is observed again, presenting an apparently multifractal character. Such multifractal phenomena were always observed irrespective of the box shape, measurement direction and strain. The slope of the line in region  $b_B$  was found to

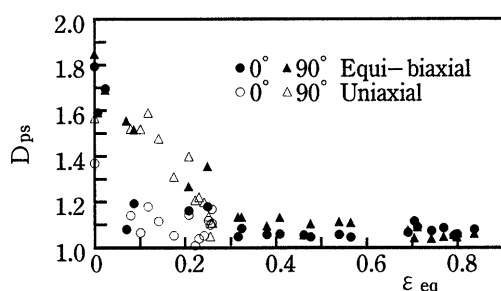


Fig. 10 Relationship between  $D_{PS}$  and equivalent strain  $\epsilon_{eq}$

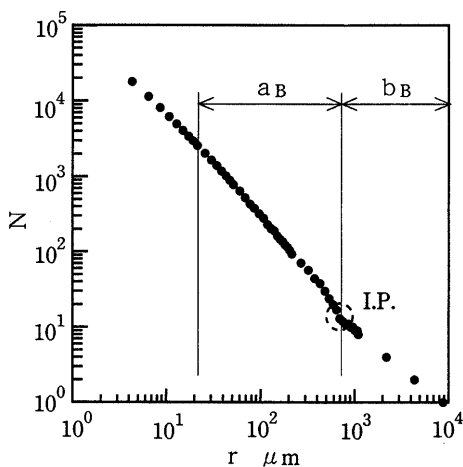


Fig. 11 Relationship between box number  $N$  and box width  $r$  in box-counting method ( $90^\circ$ ,  $\epsilon_{eq}=0.21$ , rectangular box)

be always near  $-1$  ( $D_B \approx 1$ ). This is peculiar to the box-counting method, where in the range of  $r$  exceeding a certain limit, details of the surface profiles cannot be detected and are estimated as smooth. Taking into account an error due to the geometry of the stylus profilometer, box dimension  $D_B$  was determined in region  $a_B$  with  $r$  ranging from  $10 \mu\text{m}$  to the I.P. point.

The relation between  $D_B$  and equivalent strain  $\epsilon_{eq}$  is shown for the case of rectangular boxes in Fig. 12. While  $D_B$  increases in the  $0^\circ$  direction with increasing  $\epsilon_{eq}$ , it decreases in the  $90^\circ$  direction, and then both  $D_B$  values become nearly constant beyond  $\epsilon_{eq} \approx 0.3$ . The difference in  $D_B$  between the two directions reduces with increasing  $\epsilon_{eq}$ , and here also, the fractal tends to be in-plane isotropic. Although not shown here, the  $D_B$  value in the case of the square box was found to be less than that in the case of the rectangular box, but its variation with  $\epsilon_{eq}$  was similar to the aforementioned.

The box width at the aforementioned I. P. point is denoted by  $r_{cr}$ , and its relation with  $\epsilon_{eq}$  is shown in Fig. 13. It is noted that  $r_{cr}$  increases linearly with increasing  $\epsilon_{eq}$ , followed by a steep increase. Strain  $\epsilon_{eq}$  upon the steep increase in  $r_{cr}$  is about 0.7 in equi-biaxial tension, and nearly agrees with that on localized necking initiation. A similar phenomenon to this

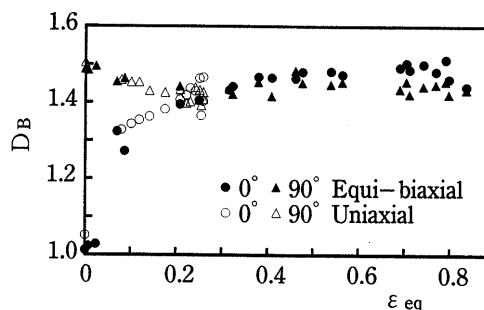


Fig. 12 Variation of  $D_B$  with equivalent strain  $\epsilon_{eq}$  (rectangular box)

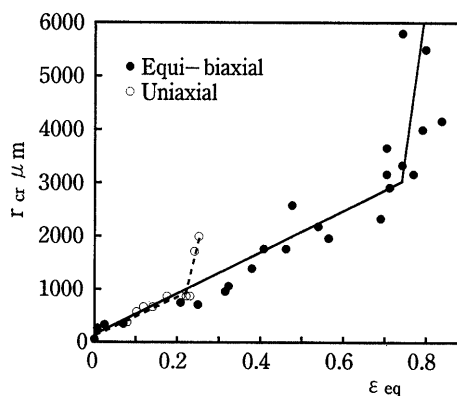


Fig. 13 Variation of critical box width  $r_{cr}$  with equivalent strain  $\epsilon_{eq}$  ( $90^\circ$ , rectangular box)

was also observed in the uniaxial tension test<sup>(4)</sup>. Such a steep increase in  $r_{cr}$  is attributable to large surface waviness caused by localized necking (see Fig. 3). Although  $R_y$  was also expected to indicate necking initiation, it did not give as good a reproducibility and as clear a result as  $r_{cr}$  did.

#### 4.5 Characteristics of surface roughening and their dependence on stress ratios

Various fractal dimensions obtained in the present experiment are summarized in Fig. 14. Results in the uniaxial tension are also added.  $\bar{D}_{PS}$  and  $\bar{D}_B$  are averages of  $D_{PS}$  and  $D_B$  in the  $0^\circ$  and  $90^\circ$  directions, respectively. They as well as  $\bar{D}_Z$  are regarded as means for expressing in-plane mean properties, and are focused on in the following discussion.

As discussed previously<sup>(4)</sup>, while  $\bar{D}_Z$  is a measure that expresses directly the complexity in surface geometries,  $\bar{D}_{PS}$  indicates the dependence of power spectra on the wavelength; thus, it is taken to be an indirect measure, because it involves the transformation of surface geometries into the power spectra.  $\bar{D}_B$ , which is easy to estimate, is also a measure related to surface complexity, and its property may be rather near to that of  $\bar{D}_Z$ . However, since  $\bar{D}_B$  attributes no unique value to self-affine surfaces<sup>(5)</sup>, it should be used for an expedient purpose. The different fractal dimensions shown in Fig. 14 have different physical meanings. However, characteristics common to all the fractal dimensions are as follows:

① Employing the equivalent strain  $\varepsilon_{eq}$  facilitates expression of strain dependence of fractal dimensions as a single curve, irrespective of the tensile method (stress ratios).

② Either of the fractal dimensions becomes constant beyond a certain strain level.

Characteristic ① is also seen in Figs. 10 and 12. Yamaguchi et al<sup>(2)</sup> carried out tensile tests while varying strain ratios, and obtained a similar conclusion with regard to surface roughness  $R_y$ . These results suggest that if macroscopic plastic work on the sheets is specified, their corresponding surface

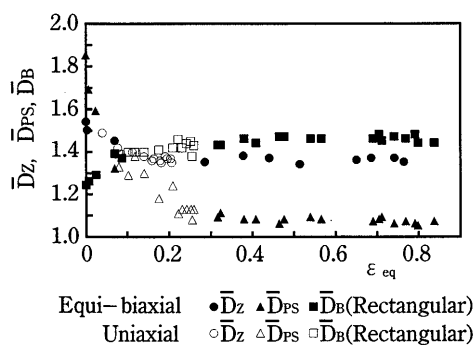


Fig. 14 Comparison among various fractal dimensions

structure is uniquely determined independent of the stress ratio. However, further investigations are required to confirm whether this rule holds in general. Characteristic ② indicates that when a surface area increases macroscopically and microscopically with increasing plastic strain and is eventually dominated by the newly formed surface, the fractal structure of surfaces becomes constant.

The  $\bar{D}_Z$  value in the steady state is found to be about 1.35. Since it is a dimension of the periphery curves of zero-set elements generated from a surface, the dimension of this original surface can be estimated as 2.35, because the surface dimension is larger by one than that of the periphery curves, as stated in section 2.1. The decrease in  $\bar{D}_{PS}$  seen before the steady state means that with an increase in surface area, spectrum components with longer wavelengths become dominant. The information on  $\bar{D}_{PS}$  is utilized for simulation of surface roughening, as mentioned in the following.

#### 5. Simulation of Surface Roughening

An attempt was made to develop a computer simulator creating surface profiles by modeling a distribution of the power spectrum and by using inverse FFT. A model of the spectrum distribution is schematically illustrated in Fig. 15. First, the relation of  $\log(S_p)$  vs.  $\log(\lambda)$  was approximated to three broken lines, referred to as a base spectrum  $S_p'$  here. The parameter  $\lambda_1$  is a wavelength at the boundary between regions  $a_{PS}$  and  $b_{PS}$  shown in Fig. 7, and a straight line was applied to the range  $\lambda \leq \lambda_1$ . From an examination in the range  $\lambda > \lambda_1$  (region  $b_{PS}$ ), an approximation to two broken lines was regarded as adequate for the purpose. The slopes of three lines and the wavelengths at the inflection points are denoted by  $\beta_1, \beta_2, \beta_3$  and  $\lambda_1, \lambda_2$  in Fig. 15, respectively.

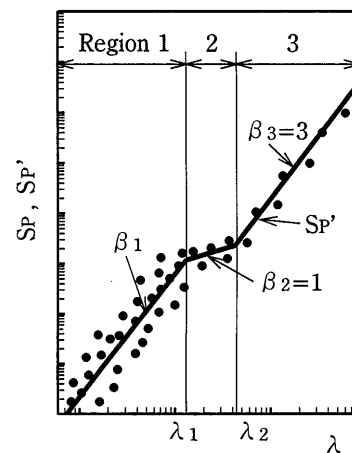


Fig. 15 Three-broken-lines model of power spectra under equi-biaxial tension

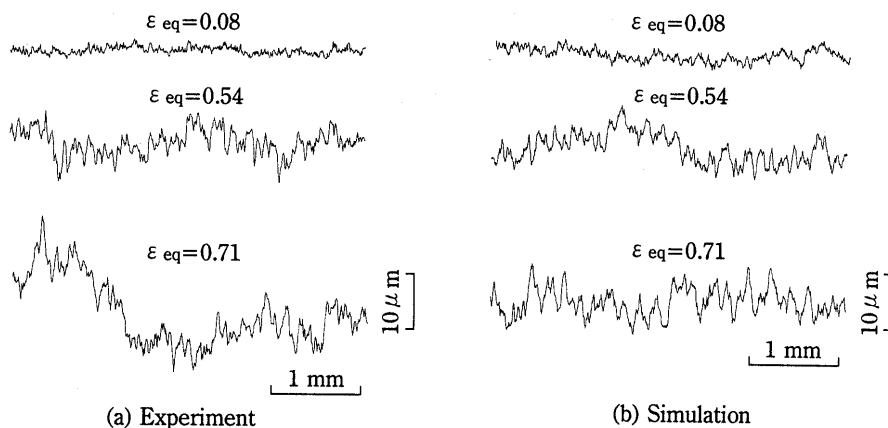


Fig. 16 Comparison of surface profiles between experiment and simulation (90°)

Second, using the following equation, the base spectrum  $S_P$  was transformed into the spectrum  $S_P$  involving such a random dispersion as shown in Fig. 9.

$$S_P = S_P^0 G^2 = 10^c \lambda^{\beta} G^2 \quad (4)$$

where  $G$  is Gaussian random number, and  $c$  and  $\beta$  are constants in each line constituting the base spectrum. The real and imaginary parts of  $S_P$ , denoted by  $A$  and  $B$ , were calculated using the following equations<sup>(11)</sup>.

$$\left. \begin{aligned} A &= S_P^{1/2} \cos(2\pi\phi) \\ B &= S_P^{1/2} \sin(2\pi\phi) \end{aligned} \right\} \quad (5)$$

where  $\phi$  is a random number ranging from 0 to 1. After  $A$  and  $B$  were determined, surface profiles were generated through the inverse Fourier transformation. According to an examination of the input parameters, the simulation accuracy improved with their values near the experimental ones. However, good results were still obtained by fixing  $\beta_2$  and  $\beta_3$  as 1 and 3, respectively. Thus, the input parameters were reduced to four ( $c$  and  $\beta_1$  in region 1,  $\lambda_1$  and  $\lambda_2$ ), and determined from the experimental data. Surface profiles created by the aforementioned method are compared with those obtained experimentally in Fig. 16, indicative of a satisfactory simulation except for the waviness accompanied by the initiation of localized necking. In this way, the validity of the present simulation has been confirmed. However, it may be said that this consequence is a matter of course, because the parameters used in the simulation have been evaluated directly by the experiment. However, although not shown here, by introducing some functions expressing the relations of the respective parameters  $c$ ,  $\beta_1$ ,  $\lambda_1$  and  $\lambda_2$  with the equivalent strain  $\varepsilon_{eq}$ , prediction of a surface profile at any specified strain was achieved.

## 6. Concluding Remarks

The results obtained in the present research are summarized as follows:

- (1) In the process of surface roughening under

uniaxial and equi-biaxial tensions of aluminum sheets, surface profiles with long wavelength components grow with increasing surface area, followed by a steady state causing a constant fractal dimension. Accordingly, the fractal structure of newly formed surfaces due to plastic deformation is regarded as constant.

- (2) The increase in plastic strain reduces the variation of fractal dimensions in the tested directions, thus making surfaces in-plane isotropic.

- (3) The box-counting method serves to sensitively detect the initiation of localized necking in both uniaxial and equi-biaxial tensions.

- (4) As a possible rule with regard to the roughness and fractal dimension of roughening surfaces, it is suggested that their strain dependence is unifiable by employing the equivalent strain, irrespective of the tensile state (stress ratios).

- (5) Based on the results of power spectrum analysis, a method for simulating surface roughening is presented, and its validity is confirmed.

## References

- (1) For example, Kienzle, O. and Mietzner, K., *Atlas Umgeformter Metallischer Oberflächen*, (1967), p. 19, Springer-Verlag.
- (2) For example, Yamaguchi, K., Nishimura, S., Takakura, N. and Hukuda, M., Thickness Dependence of Instability Strains in Uniaxial Tension of Sheet Metals, *J. JSTP.*, (in Japanese), Vol. 21, No. 237(1980), p. 909-916.
- (3) For example, Kobayashi, T. and Ishigaki, H., Granulating Behavior of Surface Texture and Deforming Limit in Press Forming, *J. JSTP.*, (in Japanese), Vol. 15, No. 158(1974), p. 197-205.
- (4) Kurosaki, Y., Matsui, M., Kitoh, T. and Takayama, T., Fractal Analysis of Free Surface Profile of Sheet Metals under Uniaxial Tension, *Trans. Jpn. Soc. Mech. Eng.*, (in Japanese), Vol. 62, No. 602, C(1996), p. 4107-4113.

- (5) Mandelbrot, B.B., Self-Affine Fractals and Fractal Dimension, *Physica Scripta*, Vol. 32(1985), p. 257-260.
  - (6) Peitgen, H.O. and Saupe, D., *The Science of Fractal Images*,(1988), p. 45, Springer-Verlag.
  - (7) Takayasu, H., *Fractal*(in Japanese), (1986), p. 18, Asakura Publishing.
  - (8) Peitgen, H.O. and Saupe, D., *The Science of Fractal Images*,(1988), p. 65, Springer-Verlag.
  - (9) Peitgen, H.O. and Saupe, D., *The Science of Fractal Images*,(1988), p. 61, Springer-Verlag.
  - (10) Woodthorpe, J. and Pearce R., *The Anomalous Behaviour of Aluminum Sheet under Balanced Biaxial Tension*, *Int. J. Mech. Sci.*, Vol. 12, No. 4(1970), p. 341-347.
  - (11) Peitgen, H.O. and Saupe, D., *The Science of Fractal Images*,(1988), p. 93, Springer-Verlag.
-